Accelerated Synthesis of Nanolayered MWW Zeolite by Interzeolite Transformation

Chemistry–A European Journal
Research Article
doi.org/10.1002/chem.202302931
Chemistry Europe
European Chemical Societies Publishing
www.chemeurj.org

Special Collection

Accelerated Synthesis of Nanolayered MWW Zeolite by Interzeolite Transformation

Peerapol Pornsetmetakul,[a, b] Ferdy J. A. G. Coumans,[b] Jason M. J. J. Heinrichs,[b] Hao Zhang,[b] Chularat Wattanakit,[a] and Emiel J. M. Hensen*[b]

Hierarchical zeolites can offer substantial benefits over bulk zeolites in catalysis. A drawback towards practical implementation is their lengthy synthesis, often requiring complex organic templates. This work describes an accelerated synthesis of nanolayered MWW zeolite based on the combination of interzeolite transformation (IZT) with a dual-templating strategy. FAU zeolite, hexamethyleneimine (HMI), and cetyltrimethylammonium bromide (CTAB) were respectively employed as Al source and primary zeolite, structure directing agent, and exfoliating agent. This approach allowed to reduce the synthesis of nanolayered MWW to 48 h, which is a considerable advance over the state of the art. Tracking structural, textural, morphological, and chemical properties during crystallization showed that 4-membered-ring (4MR) units derived from the FAU precursor are involved in the faster formation of MWW in comparison to a synthesis procedure from amorphous precursor. CTAB restricts the growth of the zeolite in the c-direction, resulting in nanolayered MWW. Moreover, we show that this approach can speed up the synthesis of nanolayered FER. The merits of nanolayered MWW zeolites are demonstrated in terms of improved catalytic performance in the Diels-Alder cycloaddition of 2,5-dimethylfuran and ethylene to p-xylene compared to bulk reference MWW sample.

Introduction

Zeolites are ubiquitously used as catalysts in important chemical processes owing to their well-defined pore and channel systems, strong acidity, and high solvothermal stability.[1] For instance, the production of aromatics, an indispensable class of chemicals in modern society for manufacturing polymers, medicine, dyes and many other products, involves the use of zeolite catalysts.[1a] Currently, such chemical processes start from non-renewable fossil resources.[1a] It is estimated that the global aromatics market will continue to grow and surpass 76 billion USD by 2025.[2] Due to the concerns about climate change, alternative technologies based on renewable resources are also being developed for the supply of sustainable aromatics. Examples of such approaches are (catalytic) fast pyrolysis of lignocellulosic biomass,[3] catalytic upcycling of plastic waste,[4] methanol-to-aromatics,[5] and Diels-Alder cycloaddition reactions involving sugar-derived furans.[6] Most of these catalytic conversion processes employ 10-membered ring (10MR) zeolite catalysts. A common strategy to improve the performance of crystalline zeolite is the reduction of the size of the crystallite domains, which reduces intracrystalline residence times and, thus, in general the enhanced catalytic performance.[7] Among the many strategies, nanolayering of zeolites into sheet form with a thickness of a few nanometers can be effective.[8] For instance, nanolayering of MWW into assemblies of a few MWW layers enhances the catalytic performance of alkylation of aromatics, the Diels-Alder cycloaddition of 2,5-dimethylfuran, and methane dehydroaromatization reactions due to shorter diffusional pathways and improved accessibility of Brønsted acid sites.[9] Likewise, nanolayering of FER zeolite resulted in enhanced catalytic performance in the oligomerization of 1-pentene to liquid fuels, (skeletal) isomerization reactions, and benzylation of toluene in comparison to bulk FER zeolite.[10]

Nanolayering can be achieved by inclusion of bulky organic molecules in the interlayer, leading to the exfoliation of the zeolite structure into very thin layers with increased accessibility.[11] Compared to this post-synthetic approach, bottom-up hydrothermal synthesis offers a simpler and broader applicable approach to obtaining nanolayered zeolites. For instance, a bifunctional diquaternary ammonium surfactant was employed to direct the formation of nanolayered MWW zeolite with crystallization times in the range of 7–31 days.[11b,12] While the adamantyl ammonium head group in this bifunctional template is thought to stabilize MWW layers by electrostatic interactions, the C_{16} hydrophobic tail leads to the separation of

[a] P. Pornsetmetakul, Prof. Dr. C. Wattanakit
School of Energy Science and Engineering
Vidyasirimedhi Institute of Science and Technology
21210 Rayong (Thailand)

[b] P. Pornsetmetakul, F. J. A. G. Coumans, J. M. J. J. Heinrichs, H. Zhang, E. J. M. Hensen
Laboratory of Inorganic Materials and Catalysis
Department of Chemical Engineering and Chemistry
Eindhoven University of Technology
P. O. Box 513, 5600 MB Eindhoven (The Netherlands)
E-mail: e.j.m.hensen@tue.nl

Supporting information for this article is available on the WWW under https://doi.org/10.1002/chem.202302931

Special Collection Part of a Special Collection celebrating the 120th anniversary of the Royal Netherlands Chemical Society

the layers during zeolite synthesis, thus exfoliating the otherwise formed bulk zeolite into nanolayers. Such templates with two functionalities need to be synthesized on purpose and often require multiple synthesis steps, rendering this approach costly. A dual template strategy would allow the use of simpler chemicals, for instance by using monoquaternary surfactants for texture control with a conventional structure directing agent (SDA) for zeolite formation. Corma and co-workers combined hexamethyleneimine (HMI) as the SDA and the cationic surfactant, N-hexadecyl-N′-methyl-DABCO, as a delaminating agent to obtain delaminated MWW zeolite using a relatively long hydrothermal synthesis of 7 days.[9b,13] The increased external surface area and better accessibility of the Brønsted acid sites could be tuned by adjusting the amount of delaminating agent in the synthesis gel. A larger amount of this component resulted in a larger fraction of MWW sheets containing single or two MWW layers in the final ITQ-2 material. The use of two templates has led to several follow-up works.[9a,b,14] Among these, dual-template synthesis using the cheap and widely available cetyltrimethylammonium ammonium (CTAB) is worthwhile mentioning. Wu and co-workers demonstrated that a combination of custom-made 1,3-bis(cyclohexyl)imidazolium hydroxide, CTAB led to a pillared multilamellar structure involving calcined ITQ-1 (MWW) seeds.[14] With complete interlayer condensation being prevented, subsequent calcination not only removes the organic modifiers but also results in a disordered arrangement of MWW nanosheets (ECNU-7). Recently, Rimer and co-workers succeeded in the synthesis of MWW nanosheets using commercially available chemicals, HMI and CTAB, as templates in 7 days.[9c] Easy-to-prepare monoquaternary templates N,N-diethyl-cis-2,6-dimethyl piperidinium and 3-ethoxyl-1-methylimidazolium were used to synthesize ultrathin FER nanosheets in the presence of F mineralizer.[10c,15] Nanolayered FER zeolite was also obtained by a dual-templating method using piperidine and cetylmethylpiperidinium bromide[10b], and N-methylpyrrolidine and 2-dimethyl-3-hexadecyl-1H-imidazol-3-ium.[10d] Fully crystalline materials could only be obtained after 5–7 days. Recently, Wu and co-workers showed that the combination of CTAB with piperidine not only leads to nanosheet morphologies but also promotes nucleation of fully crystalline FER after 5 days of hydrothermal synthesis.[16] Whilst many of these studies report benefit of the application of the nanolayered zeolites as catalysts, most involve rather lengthy synthesis procedures (typically $\geq$ 7 days), the use of customized (i.e., expensive) templates, and the occasional undesirable use of HF. Such aspects render the synthesis of nanolayered zeolites costly, energy-inefficient, and non-compliant with green chemistry considerations.[9b,c, 10c, 13, 17] Industrial manufacture of nanolayered MWW and FER zeolite catalysts requires further improvements.

There are many parameters that affect the conventional synthesis of zeolites such as the Si/Al ratio, the type and concentration of amorphous silica and amorphous alumina precursors and the use of mineralizers, which have been classified by Dusselier and co-workers.[18] In the past decade, there has also been growing attention for alternative ways to steer zeolite synthesis, i.e., by use of hydroxyl radical-assisted synthesis, interzeolite transformation (IZT), and the use of microwave heating to reduce the synthesis time and phase selectivity.[19] For instance, Yu and co-workers discovered that hydroxyl radicals generated by H_2O_2 and microwave heating can promote the formation of Si-O–Si bonds, thereby accelerating the crystallization of several zeolites and expanding the Si/Al ratio window for nanosized BEA synthesis.[19a,b] Employing ultrasonication or microwave irradiation leads to faster nucleation and shorter induction periods and improves uniform heating during aging and crystallization.[19c,d] The IZT strategy has been used to accelerate zeolite crystallization of various targeted secondary zeolite frameworks from the primary zeolite used as a nutrients source. For example, FAU and BEA can be used to obtain CHA and MFI, respectively.[20] YNU-5 and AEI zeolites are examples of zeolites that can only be obtained by IZT of FAU and BEA.[21] Although AEI can be prepared from amorphous precursors, the use of AEI seed crystals obtained by IZT of FAU is still required.[22] A benefit of IZT as an approach to modify zeolite synthesis is that it can accelerate zeolite synthesis without requiring extra equipment. For IZT, FAU and BEA are frequently used as the primary zeolites, for instance in their conversion to zeolites such as CHA,[23] AEI,[24] AFX,[25] MFI,[26] MWW,[27] and FER.[10d] The use of FAU and BEA is advantageous as they can be obtained at an industrial scale without the use of organic SDA.[28]

Most of the work on IZT focuses on the synthesis of conventional bulk zeolites with little attention so far for the formation of mesopores or hierarchical structures during zeolite synthesis. This is likely the result of a lack of detailed understanding of the assembly processes underlying IZT. An early study by Zones et al. described that moderate dissolution of the primary [B]-BEA zeolite can yield a high surface area substrate that acts as nucleation centers for AEI formation.[21c] In contrast, less desirable phases were obtained when most of the precursor was dissolved. Currently, it is thought that the transfer of composite building units (CBU) from the primary zeolite to the secondary zeolite and the higher stability of the secondary zeolite are essential aspects of the IZT approach.[29] In the past few years, several IZT cases have been described in which CBUs were found to completely disassemble during crystallization, prompting the authors to propose the involvement of secondary building units (SBU) or ring building units (RBU) such as in the IZT of BEA-to-AEI,[24] BEA-to-MFI,[20c] FAU-to-AEI,[30] and FAU-to-BEA.[31] The transfer of specific moieties from a primary zeolite has so far only been proposed for the case of FAU-to-CHA IZT where the FAU had a tailored Al distribution and where no additional Si and Al source nor a SDA were used.[23a]

A general description of the mechanism of IZT is lacking. Raman spectroscopy is frequently used to study IZT as it is sensitive to the various building units involved in zeolite synthesis. Xiao and co-workers found that the increase of 6MR units during crystallization of conventional MFI goes at the expense of FAU D6R units as monitored by UV-Raman (note that one D6R unit can disassemble into two 6MR units).[26] The same group also demonstrated that a decrease in 5MR units of primary BEA and MFI zeolites correlated with an increase of 4MR and 6MR units of the target AEI zeolite.[24] This prompted

them to conclude that 5MR units rearrange into 4MR and 6MR units before being built into AEI zeolite. Overall, it was found that 4MR units are more dominant during the IZT than 6MR units. Wakihara and co-workers showed that dealuminated FAU containing a high amount of 4MR units are essential for obtaining bulk AEI zeolite via IZT of FAU.[30] Guo and co-workers demonstrated that 4MR units are more retained than 5MR units in the solid during the IZT of BEA-to-CHA, where they obtained CHA after the complete rearrangement of 5MR units into 4MR and 6MR units in only 22 h.[23b] Complementary to these insights, a recent study combined high-energy total X-ray scattering study using pair distribution function analysis with Raman analysis mentioned that 4MR units are essential nutrients among the RBU (4MR, 6MR and 8MR units) in the induction period, prior to construction of CBU of CHA zeolite.[32] Whilst these results are made for a synthesis starting from amorphous precursors, they also emphasize a critical role of 4MR RBU.

Despite the lack of a widely accepted mechanism, recent reports showed that the IZT approach can also be employed to prepare hierarchical or nanolayered zeolites. Examples are the preparation of nanolayered FER from FAU,[10d] nanocrystalline CHA from MFI,[33] and hierarchical BEA from FAU.[31,34] Only García-Martínez and co-workers investigated the mechanism of IZT to prepare hierarchical zeolites. They proposed that 6-membered ring (6MR) units can be transferred from the primary FAU zeolite to MFI zeolite in the synthesis of (mesoporous) FAU-MFI zeolite composites, as followed from the decrease of double 6-membered ring (D6R) units of FAU along with the increase of 5MR units of MFI.[35] The same group showed that 4MR units remained in the synthesis during the synthesis of hierarchical BEA during the IZT of FAU,[31] suggesting that 4MR units are transferred from FAU to BEA. Thus, a mechanism involving RBU transfer is not only relevant to IZT of conventional (bulk) zeolite but also of hierarchical zeolites.

Herein, we explore the synthesis of nanolayered MWW zeolite by combining the concept of IZT with a dual-template strategy, aiming at substantially reducing the synthesis time against the state of the art.[9c,13] Hexamethyleneimine (HMI) and cetyltrimethylammonium bromide (CTAB) were selected as agents to respectively direct atomic structure and exfoliate the MWW layers during their synthesis, while FAU zeolite was chosen as the primary zeolite that provides the Al nutrients. It should be noted that the exfoliation of the MWW layers during their synthesis is the consequence of limiting the growth of the MWW crystal structure in the *c*-direction due to CTAB. All these chemicals are readily available, avoiding the tedious preparation of complex SDAs. As we will show, this approach offers a significant reduction in the time to prepare nanolayered MWW from 168 h to 48 h. We tracked the evolution of the solids during the MWW crystallization by a combination of several techniques aimed to understand structure, morphology, texture and surface properties. Moreover, we showed that the same approach can also be used to obtain nanolayered FER. Besides extensive characterization, we also evaluated the performance of nanolayered MWW zeolite in the Diels-Alder cycloaddition of 2,5-dimethylfuran and ethylene, which provides access to biobased p-xylene.

Results and Discussion

Synthesis

Nanolayered MWW zeolites were prepared for the first time by a bottom-up approach involving a combination of a dual templating strategy (involving SDA for zeolite formation and an exfoliating agent for separating layers) and interzeolite transformation (IZT). The former is an effective method to prepare hierarchically porous zeolites specific to some topologies, while the latter approach is known to enable or accelerate the synthesis of some zeolites.[36] Inspection of relevant literature showed that relatively long synthesis times ($>$168 h) are needed to obtain nanolayered MWW zeolite using conventional synthesis methods involving amorphous precursors (Table S1). Our strategy to shorten the hydrothermal synthesis time is based on the use of hexamethyleneimine (HMI) and cetyltrimethylammonium bromide (CTAB), which respectively act as SDA and exfoliating agent, together with H-FAU as the primary zeolite for IZT. In IZT, it is thought that certain structural building units (CBU, SBU or RBU) are retained during dissolution of the primary zeolite and used in the assembly of the secondary zeolite. Besides, H-FAU provides in our case all Al nutrient and some of the Si nutrient, the remainder being supplemented by colloidal silica (Ludox HS-40) to obtain a particular Si/Al ratio in the synthesis gel. CTAB is commercially available, making this synthesis cheaper and more attractive than other custom-made mesopore-directing agents.[9c]

We obtained bulk crystalline MWW zeolite via IZT without CTAB already after 72 h as follows from the XRD pattern in Figure 1a. The textural properties of this sample as shown in Table S2 correspond to those of bulk MWW zeolite as reported before.[37] We then explored the influence of CTAB by varying the CTAB/HMI ratio in the synthesis gel. The XRD patterns in Figure 1a show that crystalline MWW zeolite can be obtained with CTAB contents up to 6% after 72 h synthesis. A further increase of the CTAB content results in mixtures of FAU and MWW zeolites with typically more FAU being present as can be derived from the XRD pattern of MWW-7.5CTA(72)-as. This result is most likely due to the stabilization of FAU zeolite by CTAB, preventing its transformation to MWW zeolite.[38] TGA analysis of the as-synthesized MWW samples reveals that the content of organics trends well with the CTAB content (Figure 1b), which points to the inclusion of CTAB in the IZT-derived MWW zeolites. SEM images of the as-synthesized MWW samples show that most of the sheets are thinner when the CTAB content is higher than 2.5%. After calcination, the XRD patterns of MWW-xCTA(72) samples contain three reflections of (001), (101), and (102), at 7.3°, 8.2°, and 10.1°, respectively (Figure S1a), which belong to partially disordered layered MCM-22.[9c,11b,39] Ar physisorption isotherms of MWW-xCTA(72) samples show a higher Ar uptake in the relative pressure range $>$0.8 for samples prepared at higher CTAB content (Figure S1b),

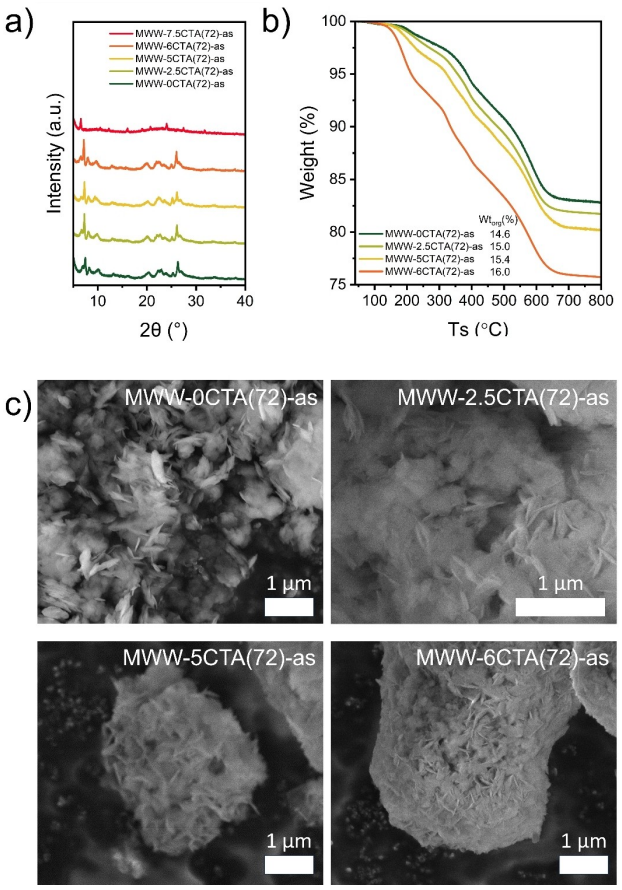

Figure 1. a) XRD patterns, b) TGA profiles, and c) SEM images of MWW-xCTA(72)-as samples.

which points to the presence of intercrystalline meso- and macropores. In contrast, the Ar uptake at low relative pressure due to micropore filling decreases with increasing CTAB content (Figure S1c). Thus, crystalline nanolayered MWW zeolite was obtained via IZT in a relatively short time of 72 h, starting from a gel containing FAU as the primary zeolite, HMI as SDA and CTAB as exfoliating agent in the range of 2.5%–7.5% to the synthesis gel, which is a considerable advance over the state of the art.

We further tracked the evolution of IZT-derived MWW zeolite by characterization of solids taken at intermediate stage of the synthesis. MWW synthesis with a CTAB content of 5% was selected for this study. Figure 2 shows XRD patterns as function of the crystallization time for MWW-5CTA(z)-as samples as well as MWW reference samples derived only from amorphous precursors (MWW-CTA(z)-amorph-as). The XRD patterns of IZT-derived samples obtained after less than 48 h synthesis contain only reflections due to crystalline FAU zeolite and a broad diffuse scattering feature typical for amorphous silica. After 48 h, a small amount of MWW (3%) can be observed together with a strong decrease of the contribution of FAU (from 100% to 5%). The MWW-5CTA(72)-as sample is fully crystalline MWW zeolite. Prolonging the synthesis beyond 72 h led to the transformation of part of MWW to FER zeolite as indicated in the MWW-5CTA(120)-as sample after 120 h (Figure 2 and Figure S2). The FAU-MWW-FER transformation sequence has also been observed during the synthesis of conventional microporous MWW zeolite via IZT (without CTAB as exfoliating agent).[27] In contrast, diffraction lines of MWW can be observed only after 120 h when the synthesis was solely based on amorphous precursors. In this case, we obtained phase-pure MWW zeolite with high crystallinity after 168 h (~84%). The onset of crystallization (induction period) of MWW derived from amorphous precursors is about 72 h, which is three times longer than for the IZT synthesis (24 h). Likewise, the crystallization period of the latter is much shorter than that of the former (~24 h for IZT vs. ~96 h for amorphous route). Thus, nanolayered MWW synthesis can be considerably accel-

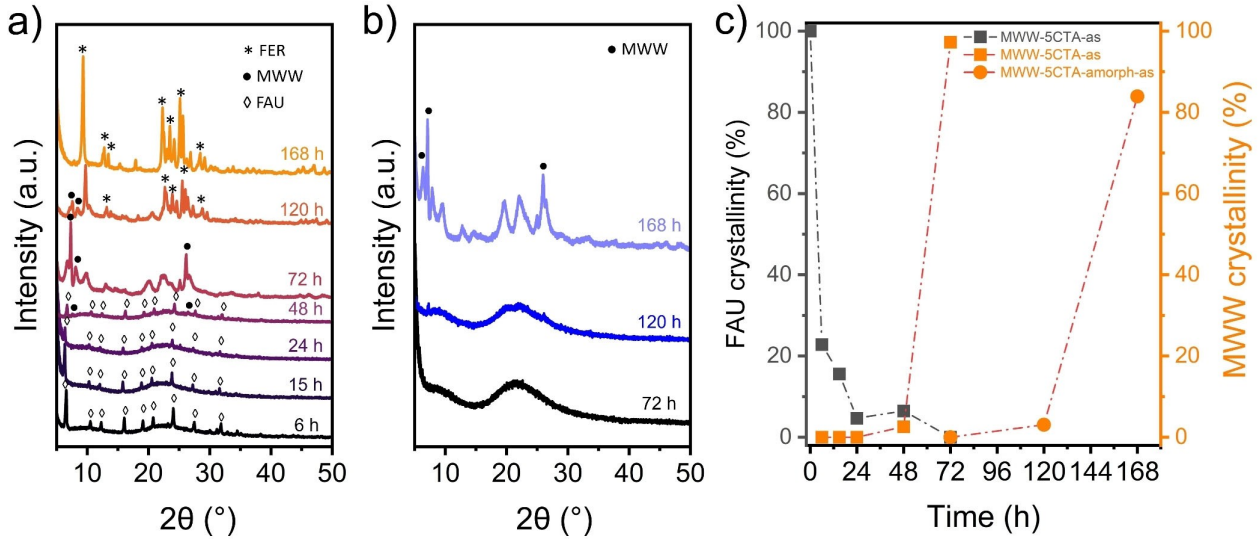

Figure 2. XRD analysis of MWW samples: a) XRD patterns of MWW-5CTA(z)-as as a function of the synthesis time, b) XRD patterns of MWW-CTA(z)-amorph-as as a function of the synthesis time and c) contributions of FAU and MWW phases during zeolite synthesis (contributions based on the changes of the area of the diffraction peaks at 2θ~6.3° for FAU and 2θ~24.5-28 ° for MWW references to the peaks areas of parent H-FAU and MWW-AP-CON-as.

erated by employing FAU as a precursor instead of amorphous precursors.

The textural properties of the MWW-5CTA samples taken at different crystallization times as determined by Ar physisorption are shown in Figure 3a, Figure S3a, and Table S2. The micropore volume, the total pore volume, the BET surface area, and the external surface area initially decrease with respect to those of the starting H-FAU precursor. When prolonging the crystallization time to 24 h, the BET surface area and the total pore volume decrease substantially. Moreover, the micropore volume is almost completely lost (< 0.01 cm^3 g^{-1}). These changes point to a complete loss of the microporous structure of the parent FAU zeolite, while the obtained materials remain (meso)porous with a significant external surface area. After 24 h, the micropore volume has the lowest value and the S_{Ext}/S_{BET} displays a maximum, indicative of a highly mesoporous material (Figure 3b). It can also be seen that the external surface area decreases the least among the other textural parameters, which hints at the transformation of the zeolite part to amorphous material. During the next 24 h, there is an increase in the micropore volume along with other parameters, underpinning the formation of crystalline zeolite, which is in line with the observation of diffraction lines of MWW zeolite after 48 h. At 72 h, the micropore volume is similar to the micropore volume of the MWW-AP-CON sample, which demonstrates the high crystallization degree (Table S2, Figure S3b). These findings show the complete FAU-to-MWW IZT into phase-pure MWW materials after 72 h crystallization, which is consistent with the XRD results.

The evolution of the morphology of the MWW-5CTA samples was investigated by SEM and TEM (Figures 3b and 4). SEM images show that the initial FAU zeolite is composed of crystals with a size smaller than 1 μm.[40] However, after 6 h of crystallization, we observe fluffy-like particles on the surface of these crystals. In addition, some of the crystals aggregate into a size larger than the initial FAU. These events are mainly due to the amorphization of the FAU precursor (Figure 3b). After prolonging the crystallization time to 15 h, the shape of the globular particles becomes irregular, which can be explained by the dissolution of the FAU and Si sources, followed by formation of new initially amorphous particles. Subsequently, the first particles with a sheet-like structure can be observed after 48 h, next to particles with an irregular shape. Agglomerated MWW nanolayers are clearly observed after a crystallization time of 72 h. Likewise, TEM images show that the nanoparticles attached to the well-defined shape bulk particles aggregate after 6 h synthesis (Figure 4). The globular particles obtained after 15 h are irregular in shape. While TEM still shows particles with an irregular shape together with nanolayered

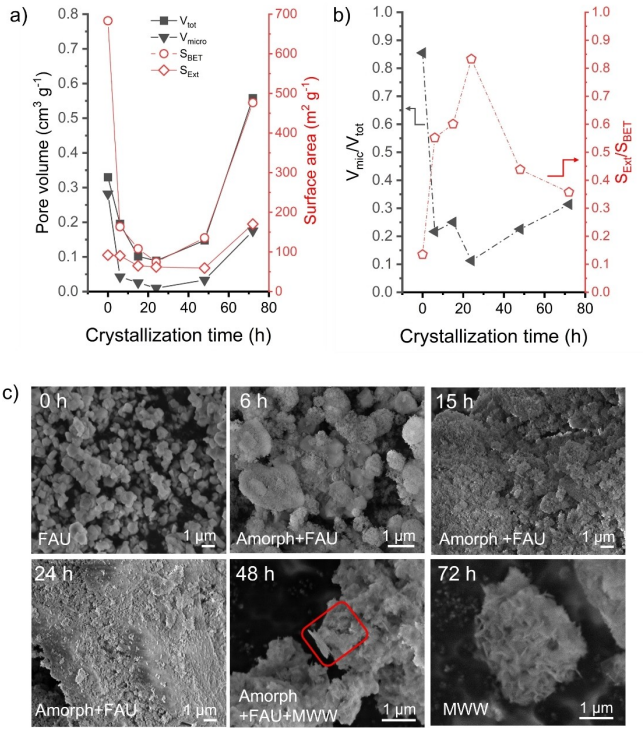

Figure 3. a) Textural properties, b) V_{mic}/V_{tot} and S_{Ext}/S_{BET} ratios and c) SEM images of H-FAU and MWW-5CTA(z) samples. H-FAU was included as the starting point at 0 h. Red-square indicates visible MWW sheet formed after 48 h.

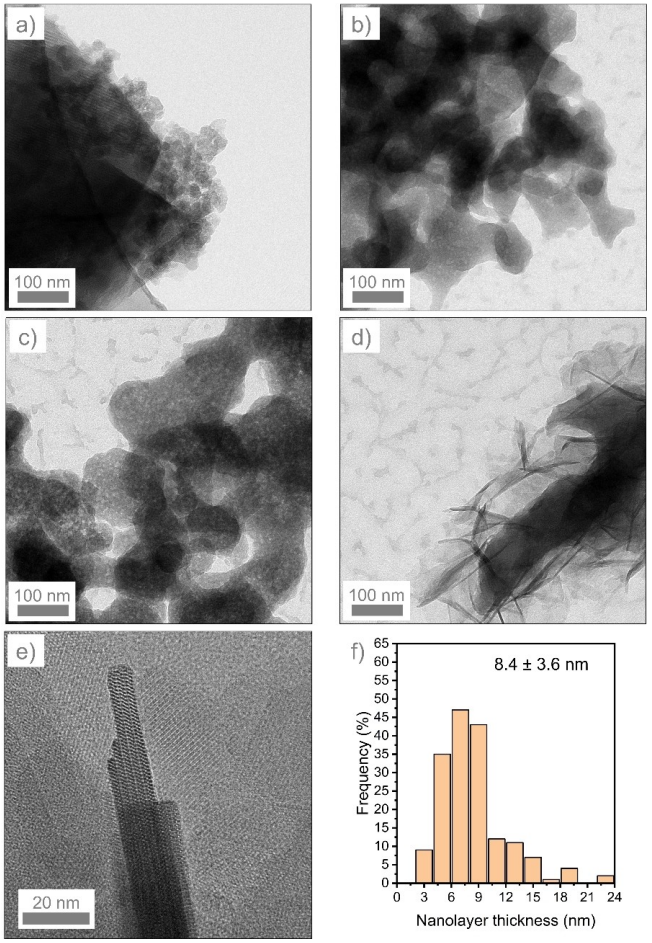

Figure 4. TEM images of a) MWW-5CTA(6), b) MWW-5CTA(15), c) MWW-5CTA(24), d) MWW-5CTA(48), and e) MWW-5CTA(72). f) The corresponding nanolayer thickness distribution of MWW-5CTA(72) determined by measurement of 171 nanolayers.

particles after 48 h, nanolayered particles can be clearly observed after 72 h. As the growth of nanolayered MWW is limited in the c-direction, the nanolayer structure cannot be very well resolved in the samples before 72 h. The average thickness of MWW layer of crystalline MWW-5CTA(72) sample is 8.4 ± 3.6 nm, which represents 3–4 MWW unit cells in the c-direction. Considering the changes in the texture and morphology, the nanolayered zeolite synthesis via IZT appears to proceed through the nearly complete dissolution of the FAU precursor before formation of nanolayered MWW zeolite occurs.

IZT can proceed via the transfer of CBU, SBU or RBU.[23a,41] To understand the underlying mechanism in the formation of nanolayered MWW from FAU, we compared the evolution of such units during MWW-5CTA synthesis by ATR-IR and Raman spectroscopy in comparison to MWW-CTA-amorph synthesis. Figures 5a and b show the ATR-IR spectra in the region of structural zeolite vibrations (550-1400 cm^{-1}). Bands due to asymmetric and symmetric T–O-T stretching modes and D6R unit can be observed at 700–1250 and 550–600 cm^{-1}, respectively.[37a] While the band at 605 cm^{-1} due to the D6R unit in MWW slowly increases during the synthesis of MWW-CTA-amorph, this unit is represented initially in the FAU sample at 590 cm^{-1} and appears in the MWW-5CTA synthesis at 605 cm^{-1} after 72 h (Figure 5a). The MWW-AP-CON sample contains this feature also, confirming its assignment to the MWW topology (Figure 5a). The solids were further characterized by Raman spectroscopy. Figures 5c and d show Raman spectra in the region of 200–800 cm^{-1}. H-FAU exhibits bands due to the D6R unit at 300 cm^{-1} and 4-membered-ring (4MR) units at 487 and 502–506 cm^{-1}.[42] Based on the Raman bands of the reference MWW-AP-CON sample and literature,[42a] the signals corresponding to 6MR units of MWW zeolite are located at 266 and 339–342 cm^{-1}, and the signal due to 4MR units of MWW is observed at 522 cm^{-1}. The broad bands of the MWW-CTA-amorph sample after 72 h in the region of 300–530 cm^{-1} are common features of amorphous aluminosilicate solids. The signals of the 6MR units of MWW appear after 120 h (Figure 5d) and the Raman characteristics due to the 6MR and 4MR units develop into similar features as in the reference MWW-AP-CON, which supports the complete crystallization after 168 h (Figure 5d). In the MWW-5CTA synthesis, the D6R unit of FAU (300 cm^{-1}) is not observed anymore after 6 h, whereas the 4MR unit of FAU (502 cm^{-1}) persists up to 48 h. This is not surprising as XRD shows that FAU remains present up to 48 h next to the presence of MWW and amorphous phases. Afterwards, the Raman bands of 6MR and 4MR units of MWW appear in the Raman spectra. The persistence of 4MR units of FAU and MWW during IZT process suggest a role of the transfer of such RBU in accelerating synthesis of nanolayered MWW via IZT as suggested before for other zeolites.[24,26,30–31]

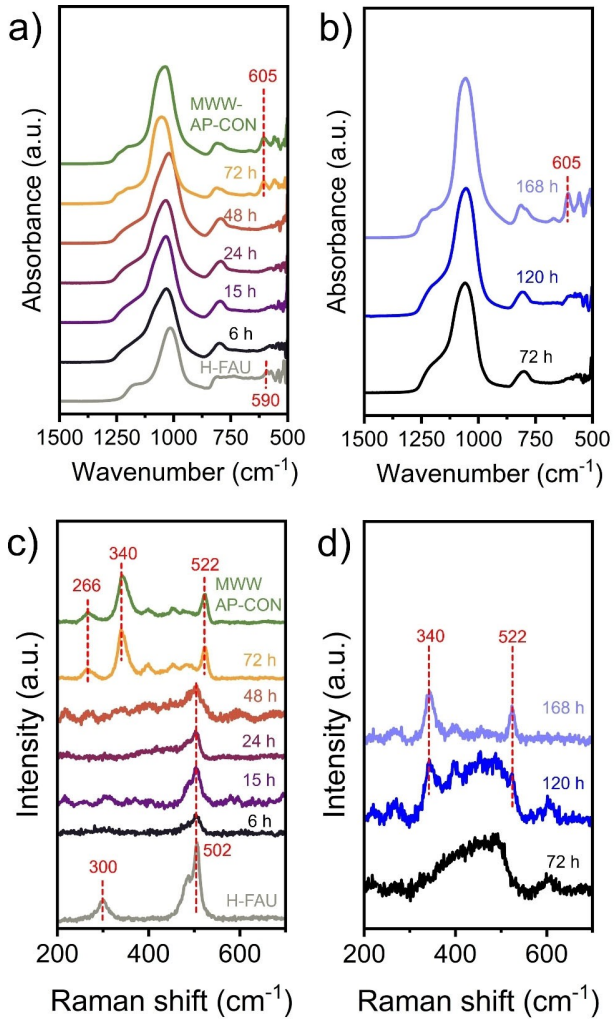

Figure 5. ATR-FTIR spectra of MWW-5CTA(z) (a) and MWW-CTA(z)-amorph (b) samples. Raman spectra of MWW-5CTA(z) (c) and MWW-CTA(z)-amorph (d) samples. ATIR-FTIR and Raman spectra of H-FAU and MWW-AP-CON were included for comparison.

We then investigated the chemical composition of the solids obtained during the synthesis by elemental analysis as well as their Si and Al speciation by ^{29}Si and ^{27}Al MAS NMR spectroscopy. The resulting data are plotted against the crystallization time in Figure 6. All solid samples exhibit higher Si/Al ratios than the Si/Al ratio in the starting gel (12.5) and in the H-FAU precursor (~2.5). The Si/Al ratio first increased from its initial value of 12.5 to a maximum of ~23.3 after 24 h followed by a decrease to ~16 after 48 h (Figure 6a). The Si/Al ratio then remains constant up to 72 h. Together with the previously discussed data, this trend can be explained by dissolution of the FAU precursor, releasing Al into the solution during the first 24 h, which is followed by Al reinsertion into newly formed phases during the next 48 h. The ^{29}Si NMR spectra shown in Figure 6b show much broader bands for the solids retrieved from the synthesis than the FAU precursor. This emphasizes the amorphous or at least less crystalline nature of these phases. According to literature, Al-rich FAU contains mostly Q^4 species with different Al distributions (i.e., (4-n)Si, nAl).[43] For the MWW-5CTA samples, the spectra were deconvoluted into contributions of Q^4 (4Si and 3Si, 1Al), Q^3 (3Si, 1OH), and Q^2 (2Si, 2OH), occurring respectively at −120 to −104 ppm, −103 to −96 ppm, and below −94 ppm (Figure 6c).[44] The fraction of Q^4 species started to increase after 15 h at the expense of Q^3 species, and became more or less constant after 48 h. These changes can be associated with the formation of

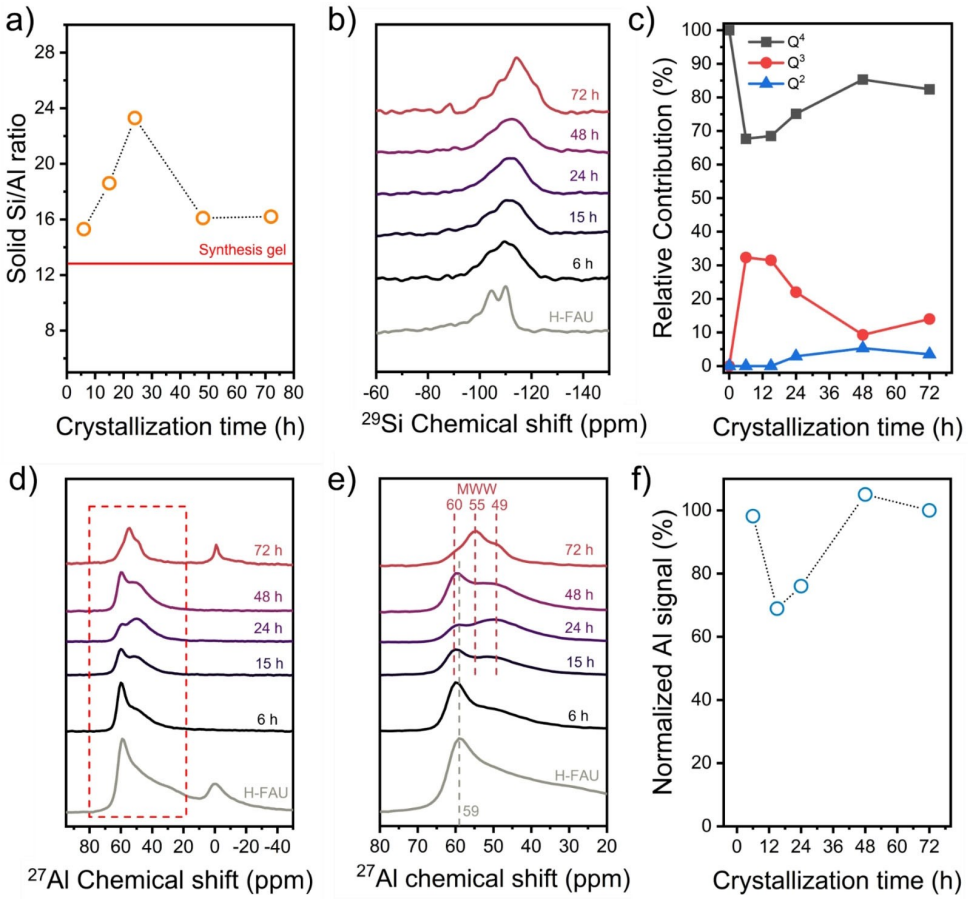

Figure 6. a) Si/Al ratio of MWW-5CTA(z) samples as determined by ICP-OES analysis, b) ^{29}Si MAS NMR, c) Si speciation in terms of Q^2, Q^3 and Q^4 species, d) weight-based ^{27}Al MAS NMR spectra, e) a zoom of the Al(IV) region of the spectra in d), and f) the total area of the weight-normalized ^{27}Al MAS signals referenced to the final MWW-5CTA(72) sample.

crystalline zeolite. Consistent with this is also the observation of a small amount of Q^2 defects, which is common for nanolayered MWW zeolite.[37b] The broad ^{29}Si NMR peaks of the MWW-CTA sample after 72 h are indicative of the layered structure of the MWW zeolite prepared by the combined dual-templating and IZT approach as compared to bulk MWW.[37b,39,45]

The ^{27}Al NMR spectra contain typical signals of tetrahedral Al (Al^{IV}) and octahedral Al (Al^{VI}) species between 45 and 60 ppm and around 0 ppm, respectively, in addition to a contribution of distorted tetrahedral or penta-coordinated Al between 20 and 40 ppm (Figures 6d and 6e).[43a,44] The starting FAU contains contributions of all three Al species. Clearly, some of the framework Al in this sample has already migrated to other positions outside the zeolite framework, which is consistent with the low stability of FAU with a high Al content.[46] Different from FAU with only one T site, MWW has 8 different T-sites.[47] Al in these sites is typically represented by a dominant Al^{IV} signal at 55 pm accompanied by shoulders at 60 ppm and 49 ppm. Already after 6 h of crystallization, all octahedral and most of the distorted tetrahedral or penta-coordinated species are not visible anymore, which is likely because they were extraframework Al species. During the synthesis, the characteristic framework Al^{IV} band of FAU at 59–60 ppm decreases, while new bands appear at 49 and 55 ppm. While after 24 h the band at 49 ppm is strongest, the band at 59 ppm is the most intense after 48 h.After 72 h, the Al^{IV} region is similar to that reported for crystalline MWW, namely with a strong signal at 55 ppm and two shoulders at 49 and 60 ppm. The evolution of these spectra points to a complex formation mechanism. Figure 6f shows the integrated Al NMR signal during the synthesis referenced to the final MWW-CTA sample after 72 h. The dissolution of Al during the initial stages of the synthesis is clear from the decrease of the Al NMR signal. The minimum is attained around 12 h. Prolonged synthesis leads to a higher Al NMR signal, which points to inclusion of Al from the solution into the new phases. The total Al signal increases up to 48 h and becomes constant up to 72 h, which coincides with the constant Si/Al ratio of the solids during this stage of the synthesis. Overall, nearly all Al from the precursor was included in the nanolayered MWW zeolites, while the solids yield of 66% for our synthesis was nearly the same as reported for hierarchical MWW synthesis by Corma and co-workers.[13] To verify the nature of the Al NMR signal in the 20–40 ppm region, we also measured ^{27}Al MQMAS NMR spectra (Figure 7). The absence of a cross peak in the MQMAS spectra in the region of 20–40 ppm implies that the samples do not contain penta-coordinated Al Thus, the

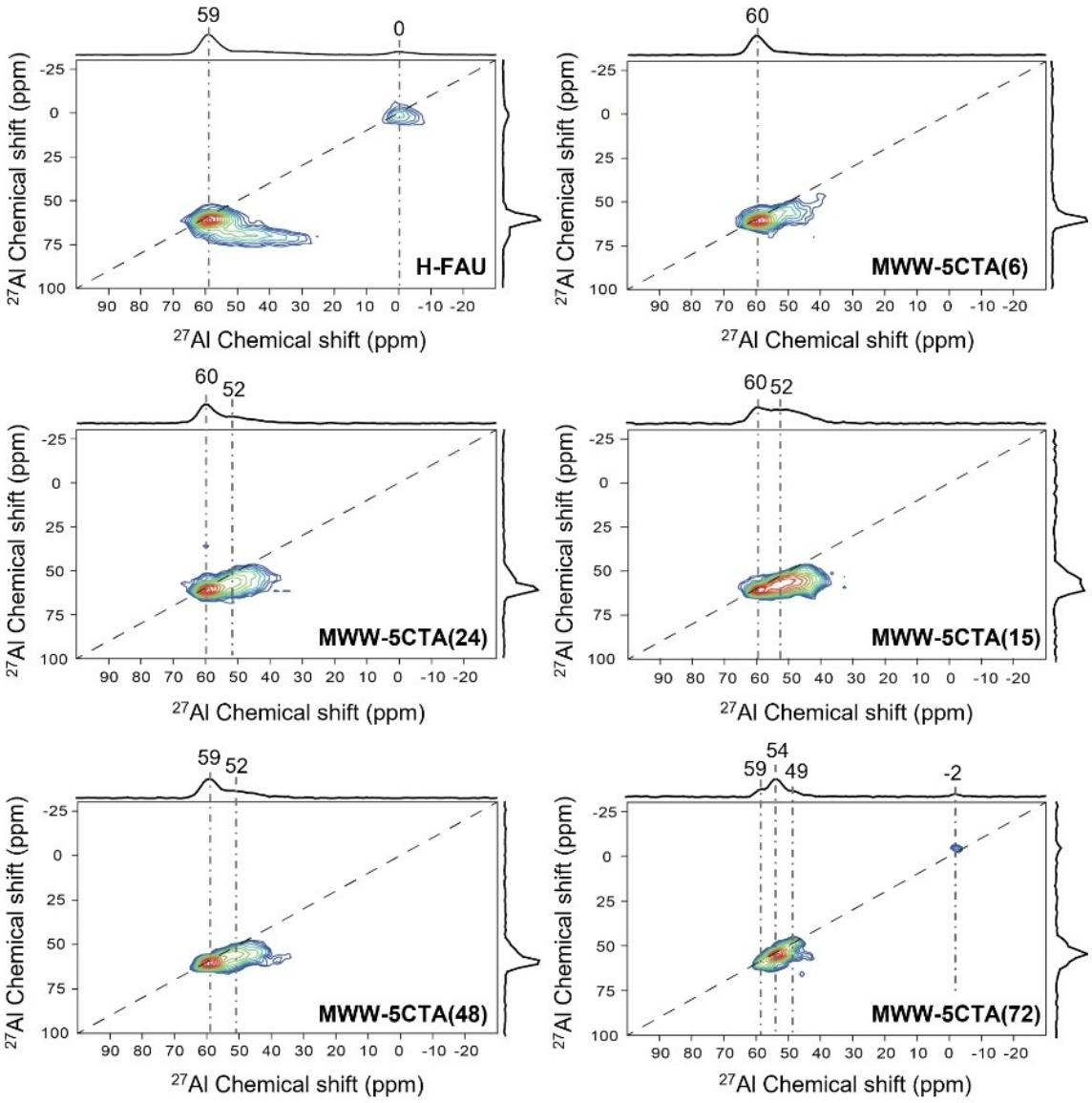

Figure 7. ^{27}Al MQMAS NMR spectra of H-FAU precursor and MWW-5CTA(z) samples.

signals are mostly due to distorted Al^{IV} species, initially part of the FAU and later in amorphous aluminosilicates.

Crystalline nanolayered MWW was obtained in the MWW-5CTA synthesis after 72 h by using colloidal silica as the main Si source. As it can be expected that the synthesis time depends on the rates of dissolution (via polymeric silica depolymerization), hydrolysis and condensation, it is worthwhile to investigate whether different Si sources can shorten the synthesis time. The properties of the used Si sources are summarized in Table S3. The hydrothermal synthesis time was reduced to 48 h. The XRD patterns and SEM images of the resulting materials show that the use of TEOS as Si source led to MFI and MOR zeolite, while fumed silica led to mixtures of FAU and amorphous products, just like the synthesis with colloidal silica (Figure 8). However, with silica gel it was possible to already obtain a pure MWW phase after 48 h. It is likely that the highly reactive nature of TEOS results in rapid crystallization of MFI followed by MOR formation after the release of Al into the gel by FAU dissolution. The higher surface area of porous silica gel compared to colloidal silica and fumed silica (Table S3) and its higher silanol density[48] make this precipitated silica more reactive, resulting in a shorter zeolite synthesis time.[49] We also repeated nanolayered MWW synthesis with silica gel using only amorphous precursors, which however only led to amorphous solids after 72 h (Figure S4). These results show the complexity of the IZT approach in which the formation of reactive Si species should be matched with the release of the Al nutrients and possibly structural motifs of the parent zeolite. Thus, also the surface area, silanol density and porosity of the Si source will impact the crystallization time and phase selectivity in the dual-template nanolayered MWW synthesis via IZT.

We also explored the possibility to prepare other Al-rich zeolites such as FER using the same gel system but with a lower Si/Al gel ratio of 7.5 using a synthesis time of 72 h. It should be

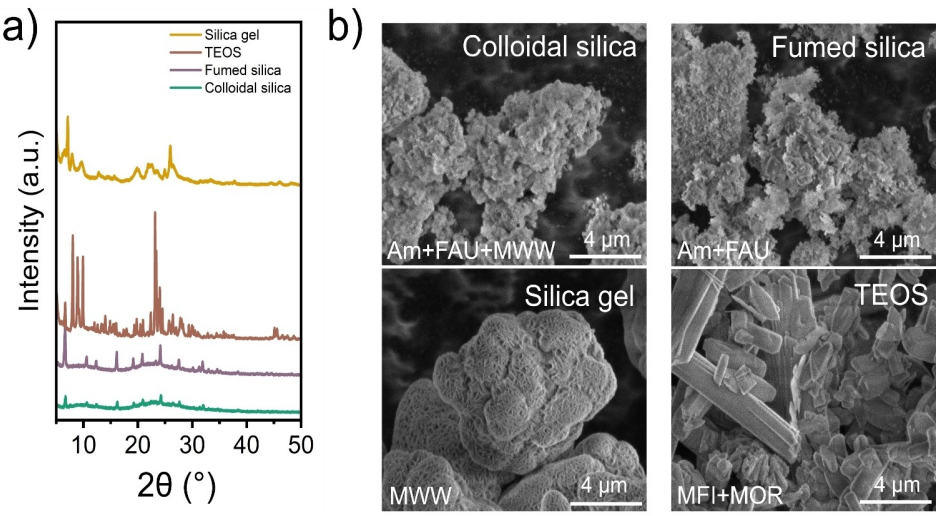

Figure 8. a) XRD patterns and b) SEM images of MWW-5CTA(48)-as samples obtained with different Si sources at the synthesis time of 48 h.

noted that HMI can also direct the formation of FER zeolite.[50] Our approach allowed obtaining FER zeolite in a synthesis with a CTAB content between 5 and 10%, whereas the synthesis without CTAB yielded a mixture of MWW and FER phases (Figure S5a). The final FER zeolite also has a nanolayered morphology and the extent of exfoliation increases when the CTAB content is increased from 5 to 10% as follows from SEM and TEM images (Figure S5b–e). This can explain the higher mesoporous volume and external surface area for the samples prepared with a CTAB content of 10% (Table S4). Earlier work reported that the addition of CTAB can accelerate the formation of FER nanolayers in a dual-template gel system using amorphous precursors and piperidine as SDA.[16] Our findings confirm that nanolayer FER formation in Al-rich gels can be accelerated in the presence of CTAB. Without CTAB, a mixture of MWW and FER zeolite was obtained via this IZT approach. We also followed the synthesis in terms of intermediate and final phases and possible building units for the FER-10CTA synthesis up to 72 h by XRD and Raman spectroscopy (Figure S6). Similar to MWW synthesis, the XRD patterns in Figure S6a show that the FER-10CTA samples contain mainly FAU and amorphous silica phases up to 48 h, while crystalline FER zeolite is observed from 72 h onwards. Figure S6b shows Raman spectra in the region of 200–800 cm^{-1} of FER-10CTA synthesis. A characteristic band due to 4MR units of FAU 502 cm^{-1}) is observed until a synthesis time of 48 h. The bands characteristic for 5MR and 6MR units in FER at ~426 and ~330 cm^{-1}, respectively, appear after 72 h. At this stage, the 4MR units of FAU are not observed anymore by Raman spectroscopy. These findings point to rearrangement of 4MR units of FAU into 5MR and 6MR units of FER as 5MR unit is not RBU of the primary FAU zeolite. Similar trends in the Raman spectra were reported during the IZT of AEI from MFI and BEA zeolites.[24] Specifically, 4MR and 6MR units of AEI were formed at the expense of 5MR units derived from the primary zeolites, which were argued to undergo rearrangement of such RBU before assembly of CBU of the final zeolite. We note that the intensity of the 5MR-related band in FER is much higher than that of the 6MR-related band of FER in the FER-10CTA sample after 72 h. The 6MR units are only formed after condensation of PREFER layers into the extended three-dimensional structure of bulk FER (Figure S6b).[11c] Overall, the Raman bands for our final FER-10CTA(72) sample shows that it represents FER layers different from PREFER in the sense that the layers are thicker. Moreover, these findings show that the combination of IZT and dual templating is also effective for obtaining nanolayered FER in an accelerated manner as compared to classical syntheses of nanolayered FER using commercially available templates, as can be judged from Table S5.

Based on characterization of structural, textural, and chemical changes during crystallization, we propose that the following main events are involved in the accelerated synthesis of MWW zeolite based on IZT in combination with a dual-template strategy (Scheme 1). The FAU precursor is slowly consumed during the induction period, resulting in the complete disappearance of D6R ring units, which leads to the release of a part of Al in the gel. Despite the nearly complete amorphization of FAU, some of the 4MR units remain intact after 48 h. These fragments are likely facilitating the nucleation of MWW zeolite after ca. 48 h, in which HMI acts as a SDA and CTAB limits the growth of the layers in the *c*-direction as also was the case in the previous work of Rimer's group.[9c] In a synthesis with the same two templates in which only amorphous precursors were used, i.e., appropriate amounts of $NaAlO_2$ and colloidal silica replacing FAU, it took 120 h before the first signs of MWW crystals were observed with 6MR units being observed before 4MR, 6MR and D6R units of MWW developed leading to full crystallization after 168 h. As such, these observations tally with those of García-Martínez and co-workers[31] and Wakihara and co-workers[32] showing an important role for 4MR units (RBU) in the crystallization of respectively BEA and CHA zeolites. Although this chain of events does not present a mechanism, it outlines the key difference observed in

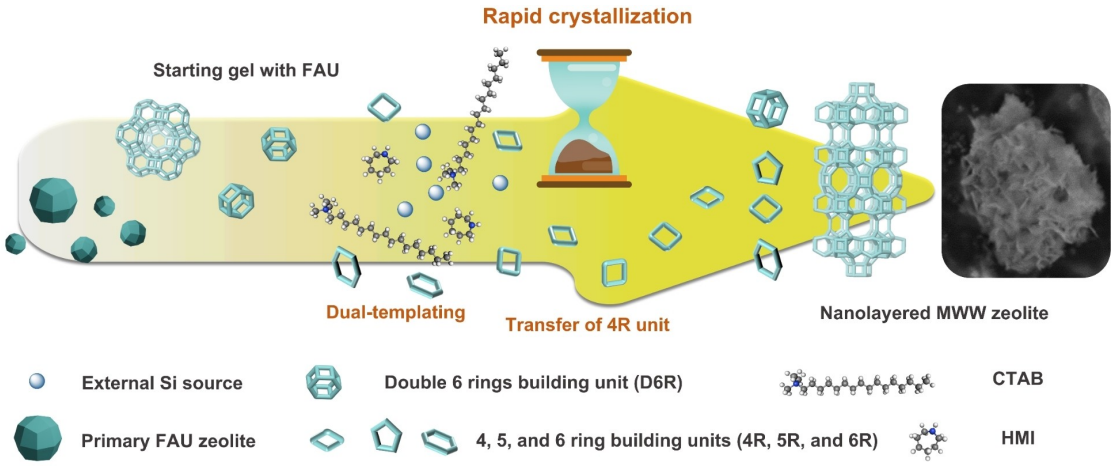

Scheme 1. Schematic representation of the key events occurring during interzeolite transformation employed to prepare nanolayered zeolite synthesis.

the synthesis with a primary zeolite in IZT as compared to a synthesis involving only amorphous precursors.

Catalytic activity

The Diels-Alder cycloaddition (DAC) of furans and ethylene to p-xylene is promising process to convert furanics, which can be readily obtained from carbohydrates, to aromatics (Scheme 2).[51] Acidic zeolites can act as suitable catalysts for this reaction.[9b,51–52] The increased external surface of nanolayered MWW zeolite as compared to its bulk counterpart leads to better accessibility of Brønsted acid sites at the hemispherical cups of the MWW surface.[9b,53] This led to improved catalytic performance in such reactions as the cracking of 4-propylphenol[54] and vacuum gas oil,[55] Friedel crafts alkylation of aromatics,[9c,13] and Diels-Alder cycloaddition of furans.[9b] Following these studies, we explored the benefit of nanolayered MWW in the DAC of 2,5-DMF and ethylene to p-xylene by comparing the performance of MWW-CTA(72) and conventional MWW-AP-CON. The DAC is a two-step reaction involving the formation of an oxanorbonene intermediate that is followed by acid-catalyzed dehydration to the final aromatic product (Scheme 2). The reaction was carried out in a batch autoclave at a temperature of 230 °C with 2,5-DMF dissolved in 1,4-dioxane and at an ethylene pressure of ~60 bar.

The numerical reaction results are given in Table S6. The reaction data show a clear benefit of the nanolayered MWW zeolites over the bulk reference. Quantification of the total BAS density by pyridine IR shows that MWW samples contain the amount of BAS in the range of 160–230 μmol g^{-1} without any obvious correlation with the CTA content. Obvious differences, however, occurred in assessing the amount of BAS located at the external surface as probed by IR spectroscopy using the larger collidine probe. The amount of external BAS was found to increase with CTA content for nanolayered MWW. Moreover, the amount of external BAS for these samples was higher than for the bulk reference and the sample obtained without CTAB, i.e., 8 μmol g^{-1} in both MWW-AP-CON and MWW-0CTA(72). The highest amount of external BAS was 21 μmol g^{-1} obtained for MWW-6CTA(72). Based on the nearly similar Si/Al ratio and framework Al fraction of these samples (Figure S7, Table S7 and S8) except for the higher Al content of MWW-AP-CON (Si/Al of 10), it is clear that hierarchization of MWW results in a higher accessibility of pores at the external surface as also known from literature.[9b,c,13,53–55] Accordingly, we correlated the obvious improved performance of the nanolayered MWW zeolites to the external surface area and the number of external BAS probed by collidine IR in Figure 9. All MWW-CTA(72) catalysts exhibited a significantly higher conversion and p-xylene yield than the bulk reference sample. Moreover, it was found that these reaction parameters improved with increasing CTA content when the CTA content was higher than 2.5 %. Overall, there is a strong correlation with the external surface area and the external BAS concentration, whereas such a correlation is absent when the activity is correlated with the total BAS density (Figure S8). Notably, the performance of MWW-0CTA(72) was comparable to that of MWW-2.5CTA(72) in line with low extent of exfoliation and the nearly similar external surface area (Fig 1c and Table S7). Nevertheless, these two samples performed better than the bulk reference with the increased *p*-xylene yield up to 40 %, which can be explained by the fact that they both exhibit a higher external surface area and, consequently, higher amount of external BAS than the bulk sample (Table S7). This example demonstrates the beneficial aspects of an accelerated synthesis based on a combination of IZT and dual templating approach for nanolayered MWW, which would be a promising

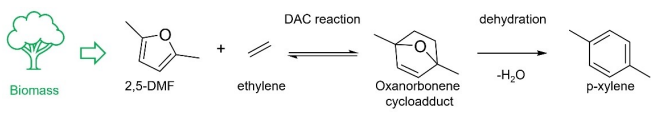

Scheme 2. Overall approach to the production of p-xylene from 2,5-dimethylfuran (2,5-DMF) with ethylene from renewable and recycled sources and the two-step nature of the Diels-Alder cycloaddition.

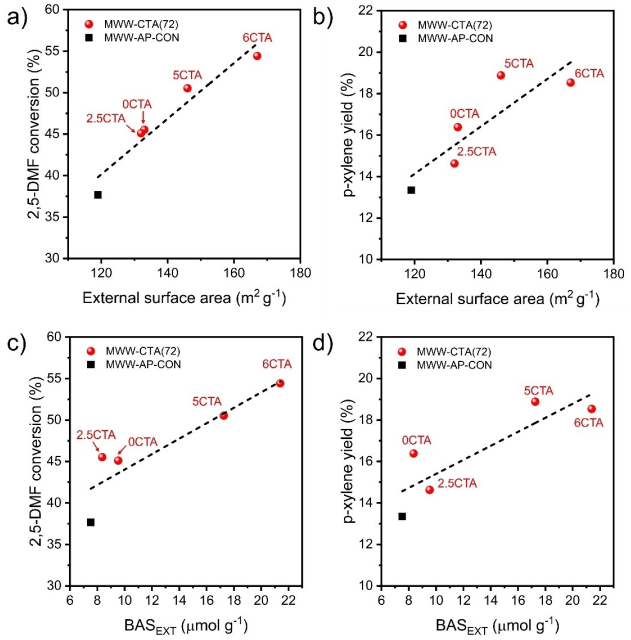

Figure 9. Correlation between external surface area and a) 2,5-DMF conversion, b) p-xylene yield. Correlation between external BAS and c) 2,5-DMF conversion, d) p-xylene yield. (Conditions: catalyst weight = 0.1 g, V = 30 mL, 2,5-DMF concentration = 1 M, T = 230 °C, p = 60 bar, time = 6 h).

catalyst for biorefinery, especially in biobased *p*-xylene production via DAC.

Conclusions

This works explores the combination of interzeolite conversion of FAU zeolite as Al source and primary zeolite with the use of a dual-templating strategy (HMI, CTAB as structure directing agent and exfoliating agent, respectively) to accelerate the synthesis of nanolayered MWW within 48–72 h, and this is the shortest synthesis period that has been reported so far (most of them require a long synthesis time up to 7 days). The evolution of the structure, texture, chemical composition, and Si and Al speciation employed to intermediate solid showed that FAU consumption was nearly complete, releasing Al nutrients that are reinserted in an amorphous precursor phase, eventually producing the MWW phase. To verify secondary building units, it was observed that 4MR units derived from FAU remain present during the formation of MWW, suggesting that such motifs play an important role in the IZT process for zeolite formation. In strong contrast to this, the absence of corresponding secondary building units during nanolayered MWW synthesis using amorphous precursors indicates that these units can facilitate the crystallization of MWW zeolite. Apart from IZT aspect, the secondary CTAB template plays a crucial role to reduce crystal growth in the *c*-direction, resulting in the formation of nanolayers. The surface area, silanol density and porosity of the Si source was also found to impact the crystallization time and the phase purity of the nanolayered MWW synthesis. Specifically, the replacement of colloidal silica by silica gel allowed further reducing the synthesis time to 48 h. Apart from MWW synthesis, the approach was applied to the nanolayered FER formation and the pure FER phase was successfully obtained using the similar scheme of synthesis period with a slight modification of synthesis procedure such as Si/Al of the starting synthesis gel. The utility of hierarchization of MWW in this way was demonstrated by the improved catalytic performance in the DAC reaction of 2,5-DMF and ethylene, which could be linked to the enhanced external surface area and accessibility of strong Brønsted acid sites. The combination of IZT and dual-template strategy thus shows potential for accelerated synthesis of nanolayered zeolite catalyst, which can be applied as a promising catalyst in *p*-xylene production from biomass-derived compounds.

Experimental Section

Materials

Colloidal silica (Ludox HS-40, Sigma-Aldrich), fumed silica (Cab-O-Sil M-5), silica gel (Davisil, 100—200 Mesh, Sigma-Aldrich), tetraethylorthosilicate (TEOS, Sigma-Aldrich), H-FAU (Si/Al = 5.1, Alfa Aesar), sodium aluminate ($NaAlO_2$, Sigma-Aldrich), sodium hydroxide (NaOH, 50 %, Sigma-Aldrich), hexamethyleneimine (HMI, TCI), cetyltrimethylammonium bromide (CTAB, Sigma-Aldrich), ammonium nitrate (NH_4NO_3, Sigma-Aldrich), 2,5-dimethyl furan (2,5-DMF, Sigma-Aldrich), 2,5-hexandione (2,5-HD, Merck), 3-methyl-2-cyclopen-1-one, (MCP, Merck) p-xylene (Merck), 1,4-dioxane (Sigma-Aldrich), and n-decane (Sigma-Aldrich) were used without further purification.

Zeolite synthesis

Nanolayered MWW and FER zeolites were obtained by interzeolite transformation as follows. In a typical synthesis, 6.21 g of double deionized (DI) water, 0.47 g of 50 wt.% NaOH, 0.97 g of hexamethyleneimine (HMI, TCI), and a desired amount of cetyltrimethylammonium bromide (CTAB, Sigma-Aldrich) were mixed at room temperature. The solution was homogenized by sonication for 20 min and then stirred overnight. An amount of H-FAU was added followed by stirring for 30 min. Then, 3.86 g of colloidal silica precursor was added to obtain a synthesis gel with the composition of 1 SiO_2: y Al_2O_3: 0.2 HMI: (x/500) CTAB: 0.18 NaOH: 15 H_2O, where y is 0.04 for MWW synthesis and 0.067 for FER synthesis. After vigorous stirring for 4 h, the gel was transferred into a 45 mL Teflon-lined stainless-steel autoclave and heated at 150 °C under rotation at 50 rpm. After reaching the targeted hydrothermal synthesis time, the autoclave was cooled to room temperature. The resulting zeolite powder was separated by centrifugation, washed by DI water until pH of filtrate < 9, and dried at 110 °C overnight. The resulting samples are denoted as MWW-xCTA(z)-as or FER-IZT-xCTA(z)-as, where x denotes the molar CTAB/HMI ratio and z the synthesis time in h. The organics retained in the samples during synthesis were removed by air calcination at 600 °C for 8 h. The calcined samples were denoted as MWW-xCTA(z) or FER-xCTA(z). The proton-form sample was obtained by ion-exchanging the calcined samples three times using a 0.5 M NH_4NO_3 solution followed by drying at 110 °C and calcination at 550 °C for 6 h. The H-MWW-xCTA(z) denotes the proton-form sample. The replacement of colloidal silica sources by other Si precursors was explored for

the synthesis of nanolayered MWW zeolite and several other Si precursors including fumed silica, silica gel and TEOS.

Nanolayered MWW zeolite was also obtained via a literature method without zeolite precursor.[9c] In brief, 0.29 g of a NaOH solution, 35.88 g of DI water, 0.21 g of $NaAlO_2$, 2.20 g of HMI, and 2.06 g of CTAB were mixed and vigorously stirred overnight. Then, fumed silica was slowly introduced to obtain a synthesis gel with the composition of 1 SiO_2: 0.033 Al_2O_3: 0.49 HMI: 0.138 CTAB: 0.18 NaOH: 43.9 H_2O. After stirring for 30 min, the gel was transferred into a 45 mL Teflon-lined stainless-steel autoclave and heated at 150 °C under rotation at 30 rpm for 168 h. The treatments afterwards were identical to those applied for MWW-xCTA(z)-as sample. The samples are denoted MWW-CTA(z)-amorph-as and MWW-CTA(z)-amorph for as-synthesized and calcined samples, respectively.

Conventional MWW zeolite synthesis via amorphous precursors (MWW-AP-CON) was synthesized following a recipe of Corma's group.[56] 0.92 g of $NaAlO_2$, 24.84 g of 1 M NaOH, 124.20 g of DI water, and 7.61 g of HMI were mixed. Then 9.23 of fumed silica (Degussa, Aerosil 200) was slowly introduced into the solution to obtain the synthesis gel with the composition of 1 SiO_2: 0.03 Al_2O_3: 0.5 HMI: 0.3 NaOH: 40 H_2O. After stirring for 30 min, the gel was transferred into a 125 mL Teflon-lined autoclave and heated at 150 °C under rotation at 60 rpm for 168 h. The following treatments were identical to those described above. These samples are denoted MWW-AP-CON-as, MWW-AP-CON, and H-MWW-AP-CON for as-synthesized, calcined, proton form samples, respectively.

Characterization

The elemental composition was determined using an inductively coupled plasma-optical emission spectrometer (ICP-OES, Spectro CirosCCD with axial plasma viewing). The samples were dissolved in a 1:1:1 (by volume) mixture of HF (40 wt.% in H_2O), HNO_3 (~60 wt.% in H_2O), and H_2O before ICP analysis. X-ray diffraction (XRD) patterns were obtained using a powder X-ray diffractometer (Bruker, New D2 phaser, Cu Kα source). Ar physisorption was carried out at −186 °C to determine the textural properties of the zeolites on a Micromeritics ASAP-2020 apparatus. Before the sorption measurements, the samples were evacuated at 360 °C for 6 h. The total pore volume was calculated at p/p_0 of 0.97. The specific surface area, micropore area, and the micropore volume were determined by Brunauer-Emmett-Teller (BET), *t*-plot methods, and non-local density functional theory (NLDFT) methods, respectively. SEM and TEM images were obtained with a field emission scanning electron microscopy (SEM, FEI Quanta 200F) and transmission electron microscopy (TEM, FEI Tecnai), respectively. TEM sample preparation involved dispersion of the powder in ethanol followed by supporting it on a Cu grid with a holey carbon film. Raman spectra of the calcined samples were recorded using a Witec alpha300 R confocal Raman microscope equipped with a Zeiss 50x/0.55 DIC objective and laser excitation with a wavelength of 532 nm at a laser power of 20 mW. The integration time for the spectra was 30 sec, and the number of scans accumulated per spectrum was 10. IR spectra of the calcined samples were measured in the range of 4000–400 cm^{-1} at a 0.5 cm^{-1} resolution averaging 32 scans by using attenuated total reflectance Fourier transform infrared spectroscopy (ATR-FTIR, Thermo Scientific Nicolet iS20 FTIR Spectrometer). Pyridine-IR and collidine-IR spectra of samples were measured on a Bruker Vertex 70v instrument in the range of 4000–1000 cm^{-1} at a resolution of 2 cm^{-1}. Each spectrum was an average of 64 scans. Typically, the thin wafer samples were placed inside a controlled-environment transmission cell. The samples were pretreated at 550 °C in artificial air before measuring the background spectra at 150 °C under vacuum. Then, pyridine or collidine was introduced into the cell from an ampoule kept at room temperature. The exposure time was ~10 min followed by desorption for 1 h under evacuation at temperatures of 150 °C, 300 °C and 500 °C. After each step, a spectrum was acquired at 150 °C. To quantify the density of acid sites in zeolites accessible by pyridine, the spectra were normalized by the weight of the wafer and molar extinction coefficient values of 0.73 cm/μmol and 1.11 cm/μmol were used for Brønsted (BAS) and Lewis acid sites (LAS), respectively.[57] To quantify the external BAS accessible by collidine, a molar extinction coefficient value of 10.1 cm/μmol was used.[58] Thermogravimetric analysis (TGA/DSC 1, Mettler Toledo) was performed to determine the organic content of the as-synthesized samples. Typically, ~4 mg of material was heated to 800 °C at a rate of 5 °C min^{-1} in an oxygen-containing flow (33 vol.% O_2 in He). Quantitative ^{29}Si magic angle spinning (MAS) NMR spectra (Bruker DPX-20) were recorded using a 4 mm diameter ZrO_2 rotor, a spinning speed of 10 kHz, and a high-power proton decoupling direct excitation (DE) pulse sequence with a 54° pulse duration of 3 μs and a recycle delay of 120 s. Quantitative ^{27}Al MAS NMR and ^{27}Al MQMAS NMR were carried out on 11.7 T Bruker DMX500 NMR spectrometer using a Bruker 2.5 mm MAS probe head and a 2.5 mm zirconia rotor spinning at 25 kHz. Prior to the ^{27}Al NMR measurements, the samples were saturated in moist air overnight.

Catalytic activity of Diels-Alder cycloaddition of 2,5-DMF and ethylene to p-xylene

Catalytic activity measurements were performed in a 0.1 L pressurized stirring-batch reactor (TOP Industrie). The catalyst was sieved (250–500 μm) prior to addition of the reaction solution. 30 mL of 1.0 M 2,5-DMF and 0.03 M n-dodecane in 1,4-dioxane was added, followed by being manually pressurized with ethylene of 25 bar (2,5-DMF:$C_2H_4 \approx 1:2.8$) at room temperature. The reaction time was started once reaching the desired temperature of 230 °C. The reaction was terminated by disconnecting the heating system, allowing it to cool down to room temperature, and subsequently depressurizing the vessel. The liquid-reaction product was separated and analyzed using a gas chromatograph (GC-FID, Shimadzu GC-17 A instrument equipped with an Rxi-5 MS column). The conversion of 2,5-DMF (X) and product yield (Y) were calculated by the following equations (1) and (2).

$$X = \frac{C_{2,5-DMF,\ reacted}}{C_{2,5-DMF,\ initial}} \times 100 \quad (1)$$

$$Y = \frac{C_i}{C_{2,5-DMF,\ initial}} \times 100 \quad (2)$$

where $C_{2,5\text{-DMF, reacted}}$ = concentration of reacted 2,5-DMF in mol L^{-1}, $C_{2,5\text{-DMF, initial}}$ = initial concentration of 2,5-DMF in mol L^{-1}, and C_i = concentration of product *i* in the reaction solution in mol L^{-1}.

Acknowledgements

The authors thank Shiyue Li, Thijs Moerkens, and Brahim Mezari of Eindhoven University of Technology, for the assistance of Raman measurement, elemental analysis, and NMR analysis, respectively. This work was financially supported by the Mitrphol group, the Vidyasirimedhi Institute of Science and Technology, Srimedhi royal scholarship from HRH Princess Maha Chakri Sirindhorn, and the National Research Council of Thailand (Mid-career Scholar Research 2023). Moreover, this

project is funded by National Research Council of Thailand (NRCT) and Vidyasirimedhi Institute of Science and Technology: VISTEC (grant number: N42 A660307). In addition, this research received financial support from Thailand Science Research and Innovation (TSRI, FRB660004/0457). This research has also received funding support from the NSRF via the Program Management Unit for Human Resources & Institutional Development, Research and Innovation (grant number: B39G660027).

Conflict of Interests

The authors declare no conflict of interest.

Data Availability Statement

The data that support the findings of this study are available from the corresponding author upon reasonable request.

Keywords: catalysis · hierarchical zeolite · interzeolite transformation · MWW · nanolayered

[1] a) W. Vermeiren, J. P. Gilson, *Top. Catal.* **2009**, *52*, 1131–1161; b) B. Yilmaz, U. Müller, *Top. Catal.* **2009**, *52*, 888–895.
[2] G. A. Market, Market Research Future, **2020**.
[3] T. R. Carlson, G. A. Tompsett, W. C. Conner, G. W. Huber, *Top. Catal.* **2009**, *52*, 241–252.
[4] Z. Dong, W. Chen, K. Xu, Y. Liu, J. Wu, F. Zhang, *ACS Catal.* **2022**, *12*, 14882–14901.
[5] T. Li, T. Shoinkhorova, J. Gascon, J. Ruiz-Martínez, *ACS Catal.* **2021**, *11*, 7780–7819.
[6] Z. Li, Y. Jiang, Y. Li, H. Zhang, H. Li, S. Yang, *Catal. Sci. Technol.* **2022**, *12*, 1902–1921.
[7] D. Kerstens, B. Smeyers, J. Van Waeyenberg, Q. Zhang, J. Yu, B. F. Sels, *Adv. Mater.* **2020**, *32*, 2004690.
[8] M. Shamzhy, B. Gil, M. Opanasenko, W. J. Roth, J. Čejka, *ACS Catal.* **2021**, *11*, 2366–2396.
[9] a) C. H. L. Tempelman, M. T. Portilla, M. E. Martínez-Armero, B. Mezari, N. G. R. de Caluwé, C. Martínez, E. J. M. Hensen, *Microporous Mesoporous Mater.* **2016**, *220*, 28–38; b) V. J. Margarit, E. M. Gallego, C. Paris, M. Boronat, M. Moliner, A. Corma, *Green Chem.* **2020**, *22*, 5123–5131; c) Y. Zhou, Y. Mu, M.-F. Hsieh, B. Kabius, C. Pacheco, C. Bator, R. M. Rioux, J. D. Rimer, *J. Am. Chem. Soc.* **2020**, *142*, 8211–8222.
[10] a) P. Wuamprakhon, C. Wattanakit, C. Warakulwit, T. Yutthalekha, W. Wannapakdee, S. Ittisanronnachai, J. Limtrakul, *Microporous Mesoporous Mater.* **2016**, *219*, 1–9; b) V. J. Margarit, M. R. Díaz-Rey, M. T. Navarro, C. Martínez, A. Corma, *Angew. Chem. Int. Ed.* **2018**, *57*, 3459–3463; c) H. Xu, W. Chen, G. Zhang, P. Wei, Q. Wu, L. Zhu, X. Meng, X. Li, J. Fei, S. Han, Q. Zhu, A. Zheng, Y. Ma, F.-S. Xiao, *J. Mater. Chem. A* **2019**, *7*, 16671–16676; d) A. Bolshakov, R. v. de Poll, T. v. Bergen-Brenkman, S. C. C. Wiedemann, N. Kosinov, E. J. M. Hensen, *Appl. Catal. B* **2020**, *263*, 118356.
[11] a) W. J. Roth, B. Gil, W. Makowski, B. Marszalek, P. Eliášová, *Chem. Soc. Rev.* **2016**, *45*, 3400–3438; b) J. Grzybek, W. J. Roth, B. Gil, A. Korzeniowska, M. Mazur, J. Čejka, R. E. Morris, *J. Mater. Chem. A* **2019**, *7*, 7701–7709; c) C. Li, M. Moliner, A. Corma, *Angew. Chem. Int. Ed.* **2018**, *57*, 15330–15353.
[12] H. Y. Luo, V. K. Michaelis, S. Hodges, R. G. Griffin, Y. Román-Leshkov, *Chem. Sci.* **2015**, *6*, 6320–6324.
[13] V. J. Margarit, M. E. Martínez-Armero, M. T. Navarro, C. Martínez, A. Corma, *Angew. Chem. Int. Ed.* **2015**, *54*, 13724–13728.
[14] L. Xu, X. Ji, S. Li, Z. Zhou, X. Du, J. Sun, F. Deng, S. Che, P. Wu, *Chem. Mater.* **2016**, *28*, 4512–4521.
[15] M. Peng, Z. Q. Wang, J. Huang, M. Shen, J. Jiang, H. Xu, Y. Ma, B. Hu, X. Q. Gong, H. H. Wu, P. Wu, *Chem. Mater.* **2021**, *33*, 6934–6941.
[16] T. Xue, S. Li, H. Wu, *Microporous Mesoporous Mater.* **2021**, *312*.
[17] A.-N. Parvulescu, S. Maurer, *Front. Chem.* **2022**, *10*.
[18] A. Deneyer, Q. Ke, J. Devos, M. Dusselier, *Chem. Mater.* **2020**, *32*, 4884–4919.
[19] a) Z. Ma, H. Deng, L. Li, Q. Zhang, G. Chen, C. Sun, H. He, J. Yu, *Chem. Sci.* **2023**; b) G. Feng, P. Cheng, W. Yan, M. Boronat, X. Li, J.-H. Su, J. Wang, Y. Li, A. Corma, R. Xu, J. Yu, *Science* **2016**, *351*, 1188–1191; c) X. Zeng, X. Hu, H. Song, G. Xia, Z.-Y. Shen, R. Yu, M. Moskovits, *Microporous Mesoporous Mater.* **2021**, *323*, 111262; d) C.-T. Chen, K. Iyoki, Y. Yonezawa, T. Okubo, T. Wakihara, *J. Phys. Chem. C* **2020**, *124*, 11516–11524; e) X. Yan, J. Zhang, T. Wang, H. Wu, L. Fang, L.-a. Liu, L. Ren, X. Guo, *Inorg. Chem.* **2023**.
[20] a) X. Xiong, D. Yuan, Q. Wu, F. Chen, X. Meng, R. Lv, D. Dai, S. Maurer, R. McGuire, M. Feyen, U. Müller, W. Zhang, T. Yokoi, X. Bao, H. Gies, B. Marler, D. E. De Vos, U. Kolb, A. Moini, F.-S. Xiao, *J. Mater. Chem. A* **2017**, *5*, 9076–9080; b) J. Zhang, J. Liang, H. Peng, Y. Mi, P. Luo, H. Xu, M. He, P. Wu, *Appl. Catal. B* **2021**, *292*, 120163; c) L. Xu, Y. Yuan, Q. Han, L. Dong, L. Chen, X. Zhang, L. Xu, *Catal. Sci. Technol.* **2020**, *10*, 7904–7913.
[21] a) Q. Liu, Y. Yoshida, N. Nakazawa, S. Inagaki, Y. Kubota, *Materials* **2020**, *13*, 2030; b) N. Tsunoji, D. Shimono, K. Tsuchiya, M. Sadakane, T. Sano, *Chem. Mater.* **2020**, *32*, 60–74; c) S. I. Zones, Y. Nakagawa, *Microporous Mater.* **1994**, *2*, 543–555.
[22] P. Hu, K. Iyoki, H. Fujinuma, J. Yu, S. Yu, C. Anand, Y. Yanaba, T. Okubo, T. Wakihara, *Microporous Mesoporous Mater.* **2022**, *330*, 111583.
[23] a) K. Muraoka, Y. Sada, A. Shimojima, W. Chaikittisilp, T. Okubo, *Chem. Sci.* **2019**, *10*, 8533–8540; b) H. Wu, Y. Lv, J. Zhang, Y. Han, C. Guo, *Microporous Mesoporous Mater.* **2021**, *328*, 111469.
[24] J. Zhang, Y. Chu, F. Deng, Z. Feng, X. Meng, F.-S. Xiao, *Inorg. Chem. Front.* **2020**, *7*, 2204–2211.
[25] C.-R. Boruntea, L. F. Lundegaard, A. Corma, P. N. R. Vennestrøm, *Microporous Mesoporous Mater.* **2019**, *278*, 105–114.
[26] J. Zhang, Y. Chu, X. Liu, H. Xu, X. Meng, Z. Feng, F.-S. Xiao, *Chin. J. Catal.* **2019**, *40*, 1854–1859.
[27] Y. Shi, E. Xing, X. Gao, D. Liu, W. Xie, F. Zhang, X. Mu, X. Shu, *Microporous Mesoporous Mater.* **2014**, *200*, 269–278.
[28] a) X. Feng-Shou, B. Xie, U. Mueller, B. Yilmaz, Google Patents, **2016**; b) P. Rani, R. Srivastava, *Chem. Rec.* **2020**, *20*, 968–988.
[29] a) K. Itabashi, Y. Kamimura, K. Iyoki, A. Shimojima, T. Okubo, *J. Am. Chem. Soc.* **2012**, *134*, 11542–11549; b) K. Honda, M. Itakura, Y. Matsuura, A. Onda, Y. Ide, M. Sadakane, T. Sano, *J. Nanosci. Nanotechnol.* **2013**, *13*, 3020–3026; c) M. Maldonado, M. D. Oleksiak, S. Chinta, J. D. Rimer, *J. Am. Chem. Soc.* **2013**, *135*, 2641–2652.
[30] Z. Liu, A. Chokkalingam, S. Miyagi, M. Yoshioka, T. Ishikawa, H. Yamada, K. Ohara, N. Tsunoji, Y. Naraki, T. Sano, T. Okubo, T. Wakihara, *Phys. Chem. Chem. Phys.* **2022**, *24*, 4136–4146.
[31] M. J. Mendoza-Castro, E. De Oliveira-Jardim, N.-T. Ramírez-Marquez, C.-A. Trujillo, N. Linares, J. García-Martínez, *J. Am. Chem. Soc.* **2022**, *144*, 5163–5171.
[32] A. Minami, P. Hu, Y. Sada, H. Yamada, K. Ohara, Y. Yonezawa, Y. Sasaki, Y. Yanaba, M. Takemoto, Y. Yoshida, T. Okubo, T. Wakihara, *J. Am. Chem. Soc.* **2022**, *144*, 23313–23320.
[33] D. Li, Y. Chen, J. Hu, B. Deng, X. Cheng, Y. Zhang, *Appl. Catal. B* **2020**, *270*, 118881.
[34] H. Ma, Z. Zhu, P. Tang, T. Su, P. Wu, H. Lü, *Microporous Mesoporous Mater.* **2021**, *311*, 110702.
[35] M. J. Mendoza-Castro, Z. Qie, X. Fan, N. Linares, J. García-Martínez, *Nat. Commun.* **2023**, *14*, 1256.
[36] T. Sano, M. Itakura, M. Sadakane, *J. Jpn. Pet. Inst.* **2013**, *56*, 183–197.
[37] a) A. Corma, C. Corell, J. Pérez-Pariente, J. M. Guil, R. Guil-López, S. Nicolopoulos, J. G. Calbet, M. Vallet-Regi, *Zeolites* **1996**, *16*, 7–14; b) A. Corma, U. Diaz, V. Fornés, J. M. Guil, J. Martínez-Triguero, E. J. Creyghton, *J. Catal.* **2000**, *191*, 218–224.
[38] a) D. Verboekend, G. Vilé, J. Pérez-Ramírez, *Cryst. Growth Des.* **2012**, *12*, 3123–3132; b) N. Linares, E. O. Jardim, A. Sachse, E. Serrano, J. García-Martínez, *Angew. Chem. Int. Ed.* **2018**, *57*, 8724–8728.
[39] J.-Q. Chen, Y.-Z. Li, Q.-Q. Hao, H. Chen, Z.-T. Liu, C. Dai, J. Zhang, X. Ma, Z.-W. Liu, *Natl. Sci. Rev.* **2020**, *8*.
[40] H. Robson, *Verified synthesis of zeolitic materials*, Gulf Professional Publishing, **2001**.
[41] K. Mlekodaj, M. Bernauer, J. E. Olszowka, P. Klein, V. Pashkova, J. Dedecek, *Chem. Mater.* **2021**, *33*, 1781–1788.
[42] a) Y. Yu, G. Xiong, C. Li, F.-S. Xiao, *Microporous Mesoporous Mater.* **2001**, *46*, 23–34; b) P. K. Dutta, K. M. Rao, J. Y. Park, *J. Phys. Chem.* **1991**, *95*, 6654–6656.
[43] a) J. Jiao, W. Wang, B. Sulikowski, J. Weitkamp, M. Hunger, *Microporous Mesoporous Mater.* **2006**, *90*, 246–250; b) H. Awala, S. M. Kunjir, V. Aurélie, J.-P. Gilson, V. Valtchev, H. Seblani, R. Retoux, L. Lakiss, C.

Fernandez, R. Bedard, S. Abdo, J. Bricker, S. Mintova, *J. Mater. Chem. A* **2021**, *9*, 17492–17501.
[44] W. Kolodziejski, C. Zicovich-Wilson, C. Corell, J. Perez-Pariente, A. Corma, *J. Phys. Chem.* **1995**, *99*, 7002–7008.
[45] A. Corma, V. Fornes, S. B. Pergher, T. L. M. Maesen, J. G. Buglass, *Nature* **1998**, *396*, 353–356.
[46] S. M. T. Almutairi, B. Mezari, G. A. Filonenko, P. C. M. M. Magusin, M. S. Rigutto, E. A. Pidko, E. J. M. Hensen, *ChemCatChem* **2013**, *5*, 452–466.
[47] G. J. Kennedy, S. L. Lawton, A. S. Fung, M. K. Rubin, S. Steuernagel, *Catal. Today* **1999**, *49*, 385–399.
[48] a) A. Burneau, O. Barres, J.-P. Gallas, J.-C. Lavalley, *Langmuir* **1990**, *6*, 1364–1372; b) B. Morrow, A. McFarlan, *Langmuir* **1991**, *7*, 1695–1701.
[49] a) Q. Wu, X. Meng, X. Gao, F.-S. Xiao, *Acc. Chem. Res.* **2018**, *51*, 1396–1403; b) W. Lei, L. Li, X. Chen, *J. Solid State Chem.* **2022**, *308*, 122899.
[50] Y. Román-Leshkov, M. Moliner, M. E. Davis, *J. Phys. Chem. C* **2011**, *115*, 1096–1102.
[51] a) Y.-T. Cheng, G. W. Huber, *ACS Catal.* **2011**, *1*, 611–628; b) C. L. Williams, C. C. Chang, P. Do, N. Nikbin, S. Caratzoulas, D. G. Vlachos, R. F. Lobo, W. Fan, P. J. Dauenhauer, *ACS Catal.* **2012**, *2*, 935–939.
[52] J. J. Pacheco, M. E. Davis, *Proc. Natl. Acad. Sci. USA* **2014**, *111*, 8363–8367.
[53] R. Barakov, N. Shcherban, O. Petrov, J. Lang, M. Shamzhy, M. Opanasenko, J. Čejka, *Inorg. Chem. Front.* **2022**.
[54] L. L. Silva, M. J. Stellato, M. V. Rodrigues, B. J. Hare, J. C. Kenvin, A. S. Bommarius, L. Martins, C. Sievers, *J. Catal.* **2022**, *411*, 187–192.
[55] A. Corma, V. Fornés, J. Martínez-Triguero, S. B. Pergher, *J. Catal.* **1999**, *186*, 57–63.
[56] A. Corma, C. Corell, J. Pérez-Pariente, *Zeolites* **1995**, *15*, 2–8.
[57] J. Datka, A. Turek, J. Jehng, I. Wachs, *J. Catal.* **1992**, *135*, 186–199.
[58] N. S. Nesterenko, F. Thibault-Starzyk, V. Montouilliout, V. V. Yushchenko, C. Fernandez, J. P. Gilson, F. Fajula, I. I. Ivanova, *Kinet. Catal.* **2006**, *47*, 40–48.

Manuscript received: September 8, 2023
Accepted manuscript online: November 20, 2023
Version of record online: December 14, 2023